

IMAGING

Rapid, Label-Free Detection of Brain Tumors with Stimulated Raman Scattering Microscopy

Minbiao Ji,^{1*} Daniel A. Orringer,^{2*} Christian W. Freudiger,¹ Shakti Ramkissoon,^{3,4} Xiaohui Liu,⁵ Darryl Lau,² Alexandra J. Golby,^{5,6} Isaiah Norton,⁵ Marika Hayashi,⁴ Nathalie Y. R. Agar,^{5,6} Geoffrey S. Young,⁶ Cathie Spino,⁷ Sandro Santagata,³ Sandra Camelo-Piragua,⁸ Keith L. Ligon,^{3,4,9} Oren Sagher,² X. Sunney Xie^{1†}

Surgery is an essential component in the treatment of brain tumors. However, delineating tumor from normal brain remains a major challenge. We describe the use of stimulated Raman scattering (SRS) microscopy for differentiating healthy human and mouse brain tissue from tumor-infiltrated brain based on histoarchitectural and biochemical differences. Unlike traditional histopathology, SRS is a label-free technique that can be rapidly performed *in situ*. SRS microscopy was able to differentiate tumor from nonneoplastic tissue in an infiltrative human glioblastoma xenograft mouse model based on their different Raman spectra. We further demonstrated a correlation between SRS and hematoxylin and eosin microscopy for detection of glioma infiltration ($\kappa = 0.98$). Finally, we applied SRS microscopy *in vivo* in mice during surgery to reveal tumor margins that were undetectable under standard operative conditions. By providing rapid intraoperative assessment of brain tissue, SRS microscopy may ultimately improve the safety and accuracy of surgeries where tumor boundaries are visually indistinct.

INTRODUCTION

The central objective in tumor surgery is to maximize tumor removal while sparing adjacent healthy tissue. Despite clear histologic differences, neoplastic tissue is often indistinguishable from healthy tissue in the operating room. Consequently, tumor is often left behind during surgery, leading to premature recurrence, treatment failure, and poor outcome. In addition, normal tissues mistaken as tumor may be removed, resulting in increased morbidity. Delineating normal tissue from tumor is particularly important in brain tumor surgery owing to the risk of neurologic deficit associated with damaging functional cerebral structures. Moreover, given the technical complexity of removing brain tumors that infiltrate into normal brain such as glioblastoma multiforme (GBM), as well as less infiltrative tumors such as metastases and meningiomas, defining an optimal surgical endpoint has been a long-standing challenge in the field of neurosurgical oncology (1–4). Extent of resection is a key prognostic factor for brain tumor patients (5–8), and the prevalence of suboptimal surgical results is surprisingly high in current neurosurgical practice (9). Consequently, tools designed to safely maximize the removal of neoplastic tissue are critically important (10).

Coherent Raman scattering microscopies, including coherent anti-Stokes Raman scattering (CARS) (11, 12) and stimulated Raman scattering (SRS) microscopy (13–16), are emerging techniques for imaging biological tissues based on the intrinsic vibrational spectroscopy of their molecular components such as lipids, proteins, and DNA

(17–21). Label-free imaging techniques are gaining acceptance within the medical imaging field because they are free from the drawbacks of dye-based methods, including heterogeneous delivery and nonspecific staining (22). In comparison to other label-free techniques, such as two-photon fluorescence, second harmonic generation, and third harmonic generation (23, 24), coherent Raman microscopy has high chemical selectivity, enabling its use in complex biological applications including brain imaging (18, 20, 25, 26). CARS and SRS have enhanced sensitivity over conventional spontaneous Raman scattering owing to the coherent nature of signal generation, enabling high-speed, real-time imaging in reflectance or epi-mode (27, 28). Moreover, the intrinsic three-dimensional optical sectioning capability of nonlinear optical microscopy is well suited for intraoperative imaging, eliminating the need for thin tissue sectioning to create a microscopic image (11, 28, 29).

SRS has several advantages over CARS for biomedical imaging, including a linear relationship between signal intensity and chemical concentration, as well as a nondistorted spectrum almost identical to that of spontaneous Raman, enabling quantitative chemical imaging (13, 17). Furthermore, by adding spectroscopic information, multi-color SRS microscopy enables the differentiation of normal and tumor-infiltrated tissues based on biochemical and morphological properties (20). Here, we show that two-color SRS microscopy can be used to detect glioma *ex vivo* in human GBM xenograft mice, with results that correlated with the interpretation of hematoxylin and eosin (H&E)-stained slides by a surgical pathologist. Most importantly, we demonstrate that SRS microscopy can detect tumor margins *in vivo* in regions that appear grossly normal under standard bright-field conditions. By enabling intraoperative microscopic, label-free imaging, SRS holds promise for improving the accuracy and effectiveness of cancer surgery.

RESULTS

SRS microscopy of mouse brain tissue

SRS (Fig. 1A) microscopy enables the visualization of tissue architecture based on the intrinsic Raman spectra of macromolecules (proteins,

¹Department of Chemistry and Chemical Biology, Harvard University, Cambridge, MA 02138, USA. ²Department of Neurosurgery, University of Michigan, Ann Arbor, MI 48109, USA. ³Department of Pathology, Brigham and Women's Hospital, Harvard Medical School, Boston, MA 02115, USA. ⁴Department of Medical Oncology, Center for Molecular Oncologic Pathology, Dana-Farber Cancer Institute, Boston, MA 02115, USA. ⁵Department of Neurosurgery, Brigham and Women's Hospital, Harvard Medical School, Boston, MA 02115, USA. ⁶Department of Radiology, Brigham and Women's Hospital, Harvard Medical School, Boston, MA 02115, USA. ⁷Department of Biostatistics, School of Public Health, University of Michigan, Ann Arbor, MI 48109, USA. ⁸Department of Pathology, University of Michigan, Ann Arbor, MI 48109, USA. ⁹Department of Pathology, Boston Children's Hospital, Harvard Medical School, Boston, MA 02115, USA.

*These authors contributed equally to this work.

†Corresponding author. E-mail: xie@chemistry.harvard.edu

lipids, etc.). Differences in Raman spectra among brain regions reflect different compositions of these macromolecules. Figure 1B shows the Raman spectra in different regions of brain including lipid-rich white matter, lipid- and protein-rich cortex, and protein-rich tumor in human brain tumor xenografts in mice. The ratio of Raman signals at 2930 and 2845 cm^{-1} (S_{2930}/S_{2845}) reflects the different lipid and protein contents. Densely cellular or solid tumor regions in mice had a mean intensity ratio of $S_{2930}/S_{2845} = 4.0 \pm 0.3$, whereas cortex and white matter had

mean ratios of 1.6 ± 0.1 and 0.93 ± 0.04 (\pm SEM, $n = 8$), respectively. We verified that the SRS signals predominantly came from the lipid and protein contents by demonstrating that Raman spectra of different brain regions (that is, white matter, cortex, and tumor) can be fit to linear combinations of lipid and protein spectra (fig. S1).

The microscope setup and the design of epi-detector for SRS imaging at reflection (epi-) mode are shown in Fig. 1C and explained in detail in Materials and Methods. In images taken at 2845 cm^{-1} (pump at 816.7 nm), nuclei and cell bodies appeared darker than surrounding extra-

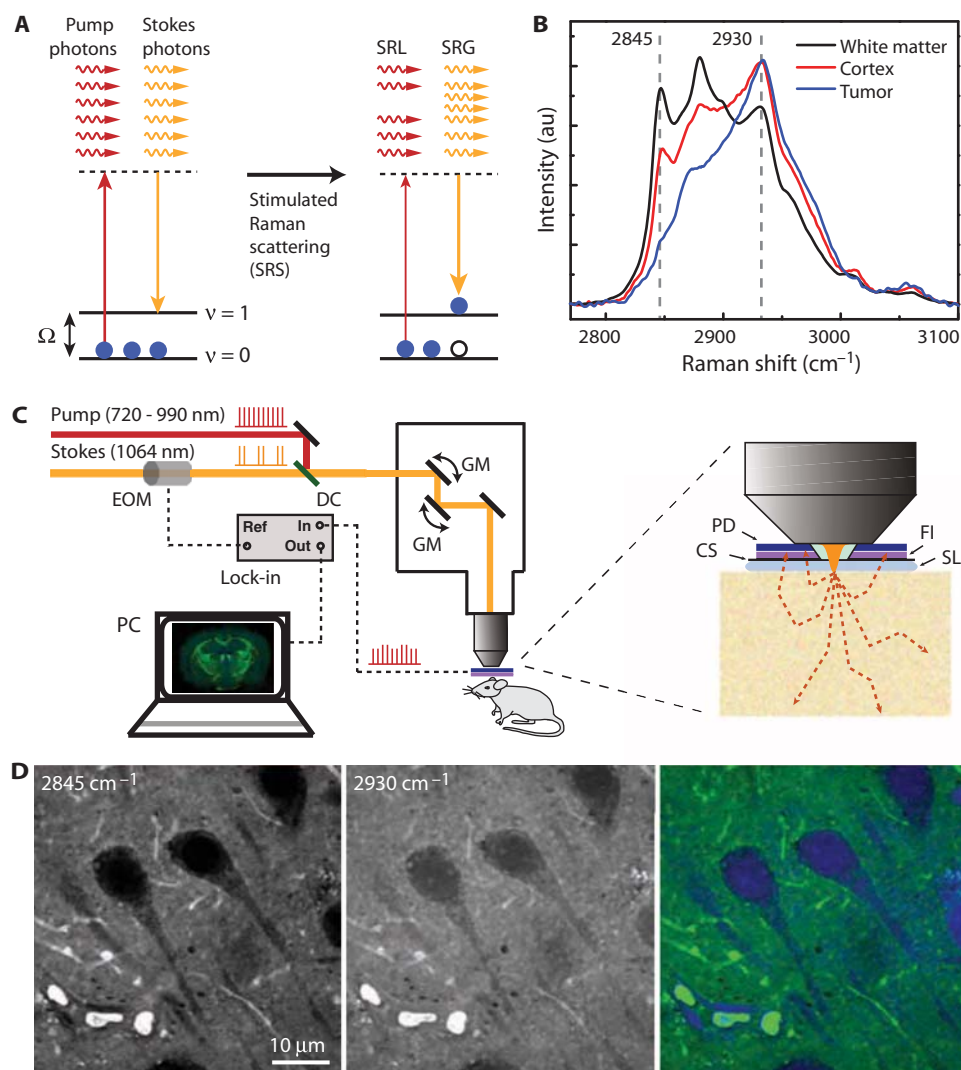


Fig. 1. Two-color SRS microscopy. (A) Energy diagram of the SRS process, where pump and Stokes photons excite the ground-state ($v = 0$) molecules to their vibrational excited state ($v = 1$), resulting in the reduction of pump intensity–stimulated Raman loss (SRL) and the increase in Stokes intensity–stimulated Raman gain (SRG). (B) Raman spectra from frozen sections of a mouse brain with human GBM xenografts show white matter, cortex, and tumor. The marked frequencies at 2845 and 2930 cm^{-1} were chosen for two-color SRS imaging. (C) Experimental setup of epi-SRS microscopy. Stokes beam was modulated at high frequency (10 MHz), and the weak SRL signal was demodulated by a lock-in amplifier. Epi-detection scheme was used for *in vivo* brain imaging and *ex vivo* imaging on fresh tissues. CS, coverslip; DC, dichroic mirror; EOM, electro-optical modulator; FI, optical filter; PD, photodiode; SL, saline. (D) Neurons in gray matter were imaged at 2845 cm^{-1} (left) and 2930 cm^{-1} (middle). A linear combination of the two raw images was used to compute the distributions of lipid (green) and protein (blue), shown in a composite image (right).

cellular structures because of the lack of lipid (Fig. 1D). In contrast, the difference in intensity between cellular and extracellular structures in images obtained at 2930 cm^{-1} (pump at 811.2 nm) was much more subtle (Fig. 1D). We used a linear combination method to extract the lipid and protein distributions (17, 20) from the two-channel images and color-coded them as green and blue, respectively (Fig. 1D). This two-color SRS imaging method mapped the proper distribution of cell bodies as well as extracellular structures, providing the structural and chemical contrast for microscopic tissue imaging.

We began by evaluating the ability of SRS microscopy to image the tissue architecture of the normal mouse brain. Thin (10 μm), unstained, snap-frozen sections were imaged nondestructively with SRS and subsequently stained with H&E and imaged with light microscopy for comparison (Fig. 2). A tiling approach was successful in collecting individual overlapping regions of interest that could be reconstructed to create a composite image of the entire imaged slice (Fig. 2A). Imaging identical sections of normal mouse brains with both SRS and H&E demonstrated the ability of SRS microscopy to detect characteristic large-scale histoarchitectural features, such as the hallmark “jellyroll” pattern of cellular layers of the hippocampus (Fig. 2B). SRS microscopy also clearly differentiated smaller-scale structural features of the brain, such as the interface between the cerebral cortex and subcortical white matter, as well as the cornus ammonis 1 (CA1) region of the hippocampus (Fig. 2C). SRS was particularly well suited for differentiating cortex from subcortical white matter at the gray/white junction owing to the strong 2845 cm^{-1} signal measured in white matter (Fig. 2D). In general, highly cellular regions within the hippocampus had high signal intensity at 2930 cm^{-1} (Fig. 2C, arrow), whereas the extracellular compartment

in the brain, including white matter tracts, tended to have high signal intensity at 2845 cm^{-1} (Fig. 2C, asterisk). Consequently, densely cellular regions appeared blue, whereas tightly packed white matter tracts appeared green. The cortex is composed of blue cells organized in a laminar fashion within a background of faintly green extracellular matrix, containing both proteins and lipid (Fig. 2C, dagger).

Unlike H&E, where contrast is generated by the binding of H&E to a range of intracellular and extracellular molecules, contrast in SRS microscopic images is related to the SRS signal intensities at 2930 and 2845 cm^{-1} . The basis of contrast in SRS microscopy explains why it is well suited for differentiating cellular regions, which have high S_{2930} and low S_{2845} , from acellular, myelin-rich regions such as fiber tracts, which have both high S_{2930} and S_{2845} . However, both SRS mi-

croscopy and H&E staining are capable of generating similar images of the microscopic architecture of tissues with tight cell-to-cell correlation (Fig. 2D, circles).

Detecting and classifying tumor-infiltrated mouse brain via SRS microscopy

The diagnosis of high-grade gliomas, such as GBM, relies on the presence of specific histologic features (dense cellularity, mitoses, microvascular proliferation, and/or necrosis) that are not present in normal brain (30). After verifying that SRS microscopy accurately captured the microscopic architecture of normal structures within the murine brain (Fig. 2), we evaluated whether it could also detect distinct histoarchitectural patterns seen in human GBM xenografts in mice. Through detailed spectroscopic measurements in the C-H stretching region, we established that Raman spectra differed substantially between tumor-infiltrated brain tissue and adjacent, non-infiltrated gray and white matter (Fig. 1B). Such spectral signatures, together with structural differences, provided the contrast between tumor-infiltrated and normal tissues.

Coronal brain sections of human GBM xenografts were imaged with both SRS and H&E microscopy for comparison (Fig. 3A). Tumor-infiltrated brain tissue was easily differentiated from the surrounding healthy tissue with SRS microscopy based on differences in cellular density (Fig. 3, B to D), the presence of infiltration within white matter bundles [tumor-infiltrated bundle (Fig. 3C, arrow); normal white matter bundle (Fig. 3C, asterisk)], and the replacement of the relatively acellular-appearing matrix of the cortex by tumor cells (Fig. 3, B and D). In many instances, SRS microscopy was capable of identifying infiltrating tumor even at low tumor density, when 25 to 75% of the field was considered infiltrated by tumor cells (Fig. 3C and fig. S2). SRS microscopy was also effective for differentiating regions of tissue with little or no tumor infiltration, where $<25\%$ of the field was infiltrated by tumor cells (Fig. 3B), and dense tumor infiltration involving $>75\%$ of the field of view (FOV) (Fig. 3D).

To quantitatively evaluate SRS as a diagnostic method for identifying tumor infiltration in specific regions of interest, we compared tumor detection via SRS and corresponding H&E microscopic images obtained from three full coronal sections of mice with orthotopic human GBM xenografts and three full coronal sections from normal mouse brains. The full SRS and H&E microscopic images were used to generate seventy-five $350 \times 350\text{-}\mu\text{m}^2$ FOVs, representing 25 FOVs from each of three categories: normal to minimally hypercellular tissue with scattered atypical cells (Fig. 3B), infiltrating glioma (Fig. 3C), and high-density glioma. A Web-based survey was populated with all 150 images (75 H&E and 75 SRS) and presented in random order. Each of the 150 FOVs (75 SRS and 75 H&E FOVs) was classified by three neuropathologists (S.S., S.C.-P., and K.L.L.), yielding a total of 450 observations. Pathologists were asked to categorize the FOVs into one of the following categories: normal to minimally hypercellular tissue with scattered atypical cells (normal) or infiltrating to high-density glioma (tumor). Results of the survey are detailed in Table 1 and table S1. Rating of H&E FOVs by neuropathologists was correct for all FOVs. There were two errors in classification of the SRS images, both in subtle distinctions: one misclassification of an FOV defined as normal to minimally hypercellular tissue with scattered atypical cells as infiltrating to high-density glioma, and one misclassification of infiltrating glioma as normal to minimally hypercellular tissue with scattered atypical cells (table S1). The κ coefficient comparing the two modal-

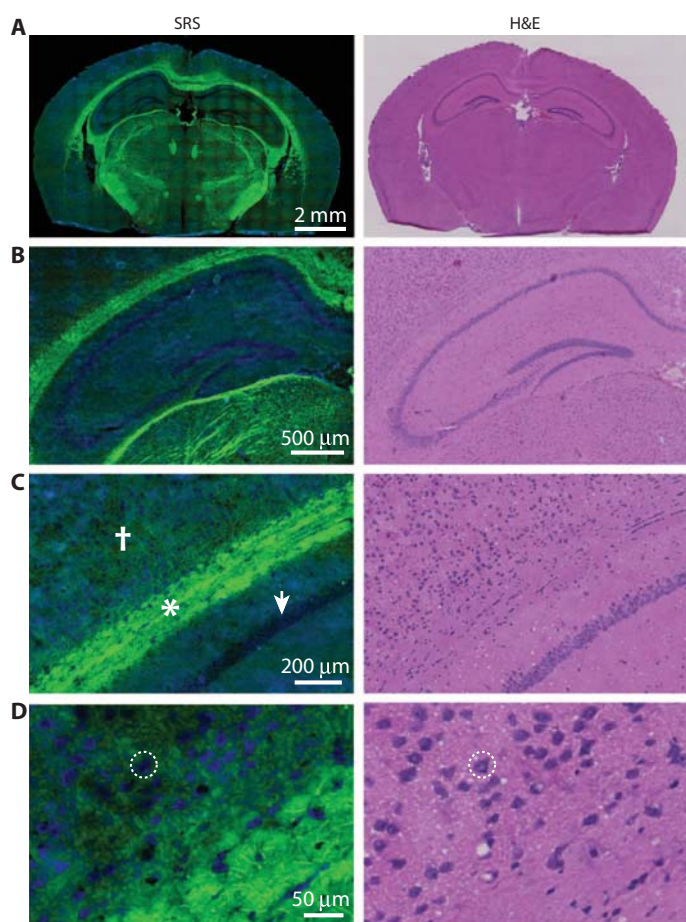


Fig. 2. SRS and H&E images of frozen normal mouse brain sections. Images are representative of six mice. Images were taken with SRS microscopy and then stained with H&E for comparison. Lipids have been false-colored green; proteins in blue. (A) Full coronal section of normal mouse brain. (B) SRS microscopy demonstrates major structural features of the normal brain, such as the hippocampus. (C) SRS microscopy differentiates regions of the brain based primarily on cellularity and the relative presence of lipids and proteins. Cortex (dagger), white matter (asterisk), and the CA1 region of the hippocampus (arrow) are readily identified. (D) The gray/white junction is evident owing to the differences in lipid concentration between cortical and subcortical tissue, with cell-to-cell correlation between SRS and H&E images (circles).

ities was 0.98 [95% confidence interval (CI), 0.95 to 0.99], demonstrating very good concordance (31) between H&E and SRS with respect to tumor detection.

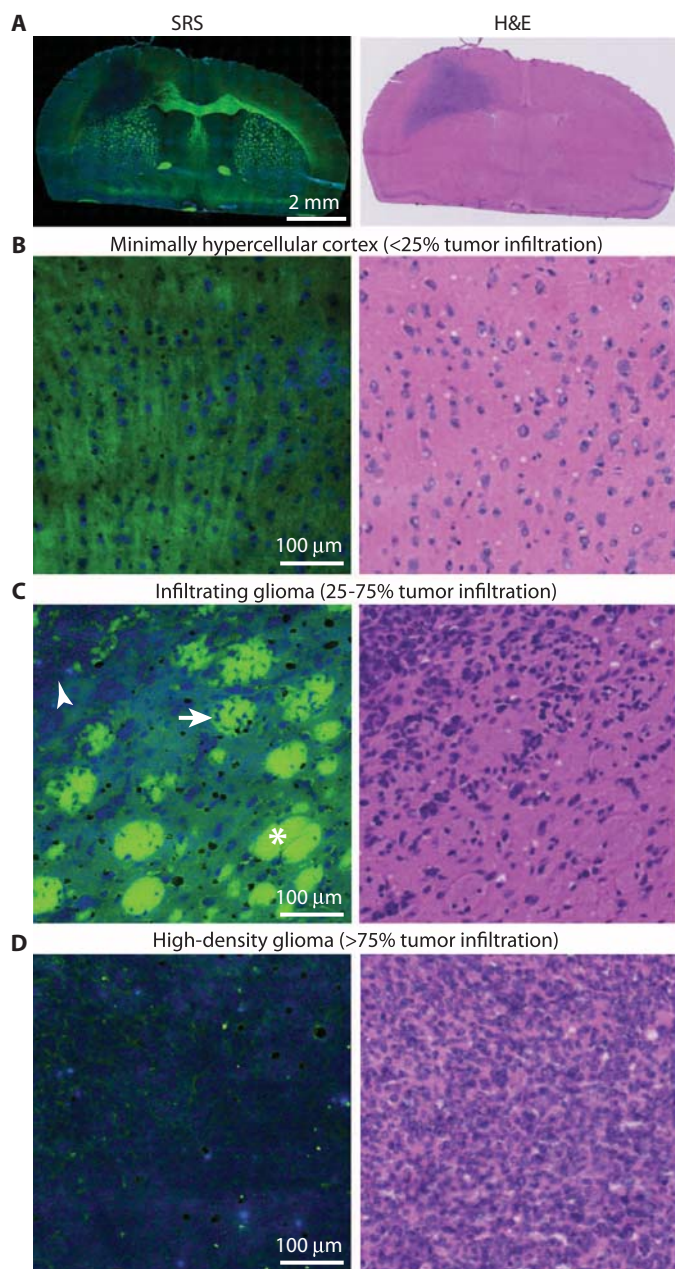


Fig. 3. SRS and H&E images of frozen human GBM xenografts. Images are representative of six mice. Images were taken with SRS microscopy and then stained with H&E for comparison. Lipids have been assigned to the green channel, and proteins to the blue channel. (A) Thin (10 μm), full section of snap-frozen brain from implanted human GBM xenograft in mice. (B) High-magnification view of normal to minimally hypercellular cortex. (C) Infiltrating glioma with normal white matter bundles (asterisk), tumor-infiltrated bundles (arrow), and dense tumor cells (arrowhead). (D) High-density glioma. FOVs similar to these were used to populate the Web-based survey to quantitatively compare SRS and H&E microscopy.

Ex vivo epi-SRS microscopy in fresh mouse brain sections

Imaging of thick, fresh tissue specimens and of tissues in situ requires reflectance or backscattering SRS imaging. We have previously demonstrated the feasibility of SRS imaging based on backscattered signal (epi-mode) (28), rather than signal transmitted through the specimen (transmission mode). To evaluate the imaging of fresh tissue, we performed epi-SRS microscopy on freshly sectioned 2-mm-thick mouse brain slices from normal mice. A comparison between transmission and epi-SRS shows similarity between the two imaging modes (fig. S3), which confirms the theoretical equivalence of transmission and epi-SRS imaging. Minor differences in the images might originate from heterogeneous light transmission and scattering across the tissue.

We focused on regions within the central nervous system that have a distinct histologic appearance and demonstrated that epi-SRS microscopy on fresh tissue sections generates images free of the artifacts associated with freezing and fixation. A comparison of Figs. 2A and 4A demonstrates differences in the imaging of fresh and frozen sections. In the frozen section, there are inconsistencies in the tissue that result in a splotchy, blue appearance throughout the SRS image as well as staining inconsistencies, related to artifacts of tissue processing (fig. S4). By eliminating the artifacts inherent in imaging frozen or fixed tissues, the histoarchitecture of the fresh mouse brain was captured with improved clarity. The expected six-layer pattern of the cerebral cortex (Fig. 4B) and the jellyroll pattern of the hippocampus (Fig. 4C) were captured in a manner that clearly depicts cellular and acellular regions. SRS imaging of white matter revealed tightly packed fiber tracts (Fig. 4D). The choroid plexus demonstrated the expected pattern of cuboidal epithelium surrounding vascular cores (Fig. 4E). In the hippocampus and dentate gyrus (Fig. 4C), SRS imaging depicted densely arched cells appearing blue surrounded by a hypocellular matrix of brain parenchyma appearing greenish. SRS imaging of hypothalamic nuclei (Fig. 4F) and habenular nucleus (Fig. 4G) reveal more evenly spaced cellular regions bordering midline ventricular boundaries. Moderately sized tracts traversing the caudatoputamen showed the ability of SRS imaging to differentiate white and gray matter (Fig. 4H).

We further investigated the use of SRS microscopy on freshly excised tumor tissue from an infiltrative GBM xenograft model (BT112) known to recapitulate many of the histologic features of human GBM (32). Using the color assignment described in Fig. 1D, the densely cellular tumor core appeared uniformly blue in comparison to the largely green appearance of surrounding hypocellular or acellular normal brain (Fig. 4I). From a structural perspective, brain tumors are characterized as hypercellular lesions, which may both displace adjacent tissues (mass effect) and infiltrate into normal gray and white matter. The blue appearance of the core of the GBM xenografts suggests hypercellularity and replacement of the greenish appearance of normal brain parenchyma, and provides a basis for distinguishing the boundaries of the tumor from the non-infiltrated regions of the normal brain (Fig. 4I). Under high magnification, tumor cells were readily apparent owing to their high nuclear-to-cytoplasmic ratio, dense growth pattern, and anaplasia (Fig. 4J).

Diffuse infiltration by small clusters of infiltrating tumor cells into brain parenchyma at the apparent margins of the tumor–gray matter interface can be readily distinguished (Fig. 4K, white dashed line). Where tumor has grown into the white matter, densely cellular, blue regions of infiltrating tumor cells dispersed throughout the green fiber tracts that are normally tightly arranged (Fig. 4L). Sampling of contiguous regions of interest from minimally infiltrated brain through the apparent tumor margin and into the tumor core (Fig. 4K, red dashed

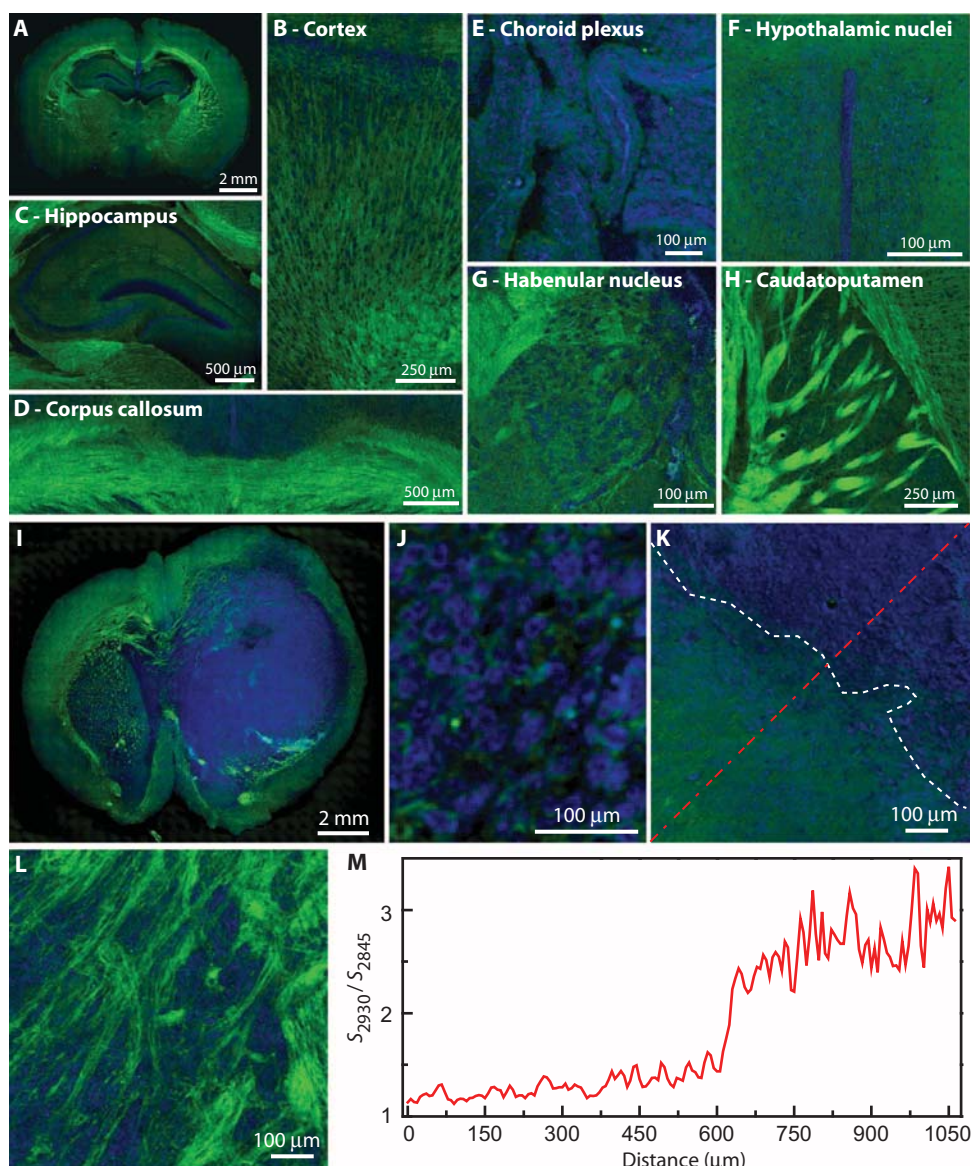
Table 1. Quantitative comparison of H&E histology and SRS microscopy. Three neuropathologists (R1, R2, and R3) reviewed a series of 75 H&E-stained tissues and 75 corresponding SRS images and recorded their

diagnoses via Web-based survey. The category indicated as “normal” in the table represents FOVs categorized as normal to minimally hypercellular tissue with scattered atypical cells.

Diagnosis		R1		R2		R3		Overall accuracy (%)
		Correct	Incorrect	Correct	Incorrect	Correct	Incorrect	
Normal	H&E	25	0	25	0	25	0	100
	SRS	24	1	25	0	25	0	98.7
Infiltrating glioma	H&E	25	0	25	0	25	0	100
	SRS	25	0	24	1	25	0	98.7
High-density glioma	H&E	25	0	25	0	25	0	100
	SRS	25	0	25	0	25	0	100
Total		149	1	149	1	150	0	99.5

Fig. 4. Epi-SRS images of fresh brain slices from normal mice and the human GBM xenograft (BT112) mouse model.

(A to L) Images are representative of 10 normal mice (A to H) and 6 BT112 mice (I to L). Lipids have been assigned to the green channel and proteins to the blue channel. Fresh 2-mm-thick coronal section of normal mouse brain. Structural features of the full section from a normal mouse (A), cortex (B), hippocampus (C), corpus callosum (D), choroid plexus (E), hypothalamic nuclei (F), habenular nucleus (G), and caudatoputamen (H) demonstrate the expected histoarchitectural patterns. In contrast, fresh 2-mm-thick coronal brain section of a BT112 human glioblastoma xenograft-bearing mouse reveals normal, green-appearing brain parenchyma surrounding blue hypercellular tumor (I). High magnification of the tumor core reveals individual tumor cells (J). The tumor–gray matter interface (white dashed line) demonstrates an invasive pattern of tumor growth (K). The tumor–white matter interface demonstrates the ability of tumor cells (blue) to traverse and separate white matter bundles (green) (L). (M) A line profile of S_{2930}/S_{2845} across the gray matter–tumor interface in (K) (red dot-dashed line) shows higher S_{2930}/S_{2845} with increasing tumor density.



Downloaded from stm.sciencemag.org on September 4, 2013

line) demonstrated a trend toward higher S_{2930}/S_{2845} with increasing tumor density (Fig. 4M). SRS images of fresh brain slices from other GBM cell lines and non-GBM mouse models are also shown (fig. S5) to demonstrate the applicability of our method to other experimental human tumor models.

In vivo epi-SRS brain tumor microscopy

To determine whether SRS microscopy was feasible in vivo, we used an infiltrative human GBM xenograft mouse model to recapitulate the irregular, diffuse border of human gliomas. In six mice, we generated human GBM xenografts that grew to the cortical surface. Craniectomies exposed the tumor engraftment site as well as adjacent non-invaded brain tissue so that we could apply a coverslip to create a “cranial window” for the SRS imaging system. The cortical surface was imaged through a cranial window. SRS image acquisition used a total laser power of ~150 mW, which could in principle be reduced (fig. S6).

The pattern of arachnoidal and pial vessels on the surface of the normal brain was clearly identifiable in both the standard bright-field and SRS images (Fig. 5A). The movement of individual blood cells through vessels captured in the SRS images results in a blurred appearance within the vessel lumina. Differences in the vascular patterns between the images are related to vessels existing superficial to the thin optical sectioning plane captured by SRS imaging. There was no gross evidence of tumor on the surface of the brain using standard bright-field microscopy (Fig. 5A, left). However, some regions of brain tissue that appeared grossly normal under bright-field microscopy demonstrated extensive tumor infiltration on SRS microscopy (Fig. 5A and fig. S7). As expected from ex vivo imaging, infiltrating tumor margins were readily visible when SRS microscopy was performed in vivo. The tumor margin (Fig. 5A, dashed line) was discernable from both a biochemical and struc-

tural perspective, with GBM xenograft tissue appearing blue and cellular (Fig. 5, B and C).

Within non-infiltrated (normal) brain tissue, normal axonal processes and the vascular pattern characteristic of non-infiltrated cortex were visible (Fig. 5D, movie S1, and fig. S7). The features of both tumor-infiltrated and non-infiltrated cortex varied with image depth. A 100- μm -depth stack, acquired from superficial to deep, near a tumor-brain interface demonstrated a transition from hypercellular, blue tumor superficially to hypocellular green cortex with intermixed linear structures, most likely representing astrocytic processes in the deeper portion of the sample (movie S1).

Differences in tumor infiltration seen during SRS imaging were also confirmed by H&E histology after in vivo imaging (fig. S8). The H&E-stained sections were acquired from a coronal plane perpendicular to the imaging planes in Fig. 5. In the H&E images, basophilic hypercellular tumor tissue can be seen originating in the cortex, extending upward to cover the surface of the hemisphere, and downward toward the corpus callosum (fig. S8). Although tissue movements caused by the respiratory and cardiac cycles resulted in a slight degradation in image quality in comparison to ex vivo SRS imaging, we were still able to identify individual cells at the tumor-brain interface (Fig. 5C). We hypothesize that the individual cells are likely neoplastic given the paucity of cells at this imaging depth in normal cortex.

We also confirmed that similar histoarchitectural features could be appreciated in simulated surgical conditions (Fig. 6). Before dissection, the surface of the brain appears acellular with frequent subarachnoid and pial vessels (Fig. 6A). Deep (about 1 mm) dissection was then carried out in the surgical field to simulate the manipulation of tissues that occurs during human brain tumor resection. Under these simulated surgical conditions, we were able to appreciate the interface between tumor and normal brain (Fig. 6B), as well as the normal-appearing white matter and cortical architecture that would be seen after tumor resection (Fig. 6C).

Ex vivo imaging of fresh human brain tumor specimens

To test the hypothesis that SRS microscopy could detect differences between tumor-infiltrated and non-infiltrated human brain, we imaged several fresh specimens removed during the course of a recurrent glioblastoma resection. The portions of the tissue removed from the patient were mounted on slides, entirely unprocessed and imaged with transmission SRS microscopy. SRS images corresponded well with similar regions imaged by traditional H&E histology (Fig. 7). As in human glioblastoma xenografts, glioblastoma-infiltrated human brain demonstrated hypercellularity (Fig. 7A) compared to non-infiltrated or minimally infiltrated areas (Fig. 7B). In addition, key diagnostic features were present in the human surgical specimens, including cellular and nuclear pleomorphism (Fig. 7C), pseudopalisading necrosis (Fig. 7D), and microvascular proliferation (Fig. 7E).

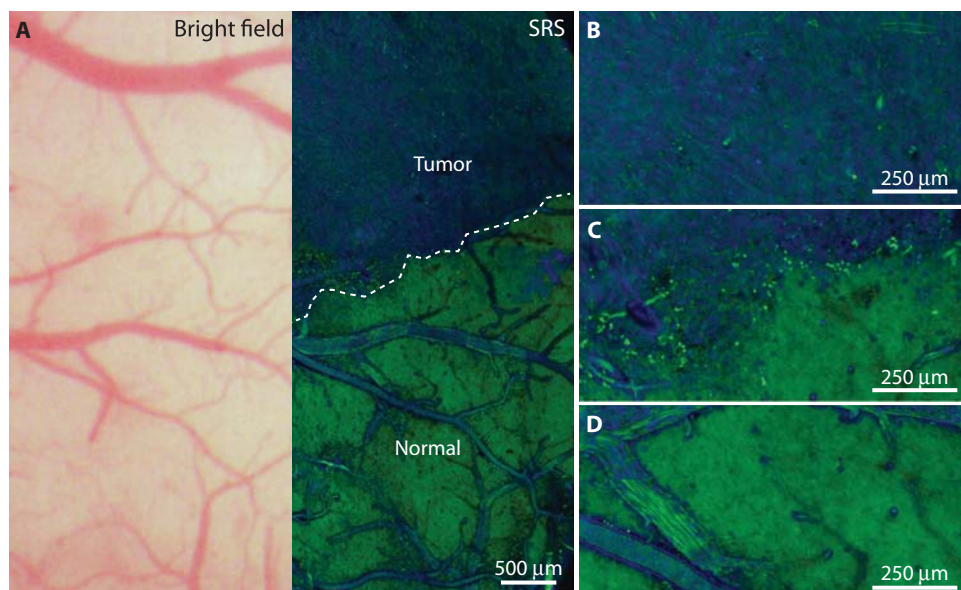


Fig. 5. In vivo SRS microscopy images of human GBM xenografts. Images are representative of six mice. SRS imaging was carried out via acute cranial window preparation in mice 24 days after implantation of human GBM xenografts. (A) Bright-field microscopy appears grossly normal, whereas SRS microscopy within the same FOV demonstrates distinctions between tumor-infiltrated areas and non-infiltrated brain (normal), with a normal brain-tumor interface (dashed line). (B to D) High-magnification views within the tumor (B), at the tumor-brain interface (C), and within normal brain (D).

DISCUSSION

Here, we provide the first evidence that SRS microscopy can be used to delineate tumor tissue in a human GBM xenograft mouse model, both *ex vivo* and *in vivo*, and in human brain tumor surgical specimens. Because it is possible to perform SRS microscopy and H&E microscopy on the same tissue sections, we were able to define the relationship between SRS and H&E microscopic images. SRS microscopy depicted much of the histologic information conveyed by H&E microscopy without the need for thin sectioning or tissue staining. SRS also provided biochemical distinction between normal and tumor-infiltrated tissues by highlighting differences in the S_{2930}/S_{2845} ratio. SRS images demonstrating densely arranged cells and a high S_{2930}/S_{2845} ratio are suggestive of regions with extensive tumor infiltration on H&E. In contrast, SRS images demonstrating normal cerebral histoarchitectural features (regularly spaced multilayered neuronal cell bodies, glial components of white matter, axonal and astrocytic processes, and white matter bundles) and a low S_{2930}/S_{2845} ratio are suggestive of non-infiltrated tissues on H&E microscopy.

Although SRS microscopy does not reveal all of the architectural, genetic, and biochemical data that can be gleaned from thin section analysis, it is well suited for differentiating normal brain from regions infiltrated by tumor based on structural features and S_{2930}/S_{2845} ratiometry. Alternative Raman bands might be used to delineate tumor from normal brain as well. For example, we have recently demonstrated that the Raman band at 1080 cm^{-1} could serve as a marker for nucleic acids to image cell nuclei with high specificity (21). However, its relatively weak Raman intensity has hindered the 1080 cm^{-1} band from being a favorable probe in *in vivo* applications. In contrast, the C-H stretching region including 2930 and 2845 cm^{-1} bands are among the strongest Raman bands in biological specimens, providing sufficient signal/noise ratio for high-speed SRS imaging. Ideally, a strong tumor-specific Raman band based on one or more chemical species that are unique to tumor cells would provide the best means for delineating normal and tumor-infiltrated regions. However, given the inter- and intratumoral biochemical variability and the limited Raman spectral differences between normal and tumor cells, it is unlikely that such a band exists.

In our study, SRS microscopy performed well for detecting human GBM tumor infiltration in mice, especially in densely tumor-infiltrated FOVs. Classification of the tumor infiltration status of FOV in this study was based primarily on disruption of normal histoarchitectural motifs, such as cortical layers and white matter bundles, as well as an assessment of cellular density. Whether H&E or SRS is used, it is difficult to definitively classify a given cell as neoplastic or nonneoplastic based on morphology alone. Nonetheless, by enabling classification of tissue through histoarchitectural criteria, SRS creates the possibility of rapid delineation of tumor-infiltrated tissues. If applied to the surgical setting, SRS could be used to redefine surgical endpoints based on microarchitectural data rather than the notoriously unreliable gross visual and textural cues that are widely used by surgeons today (8, 9, 33).

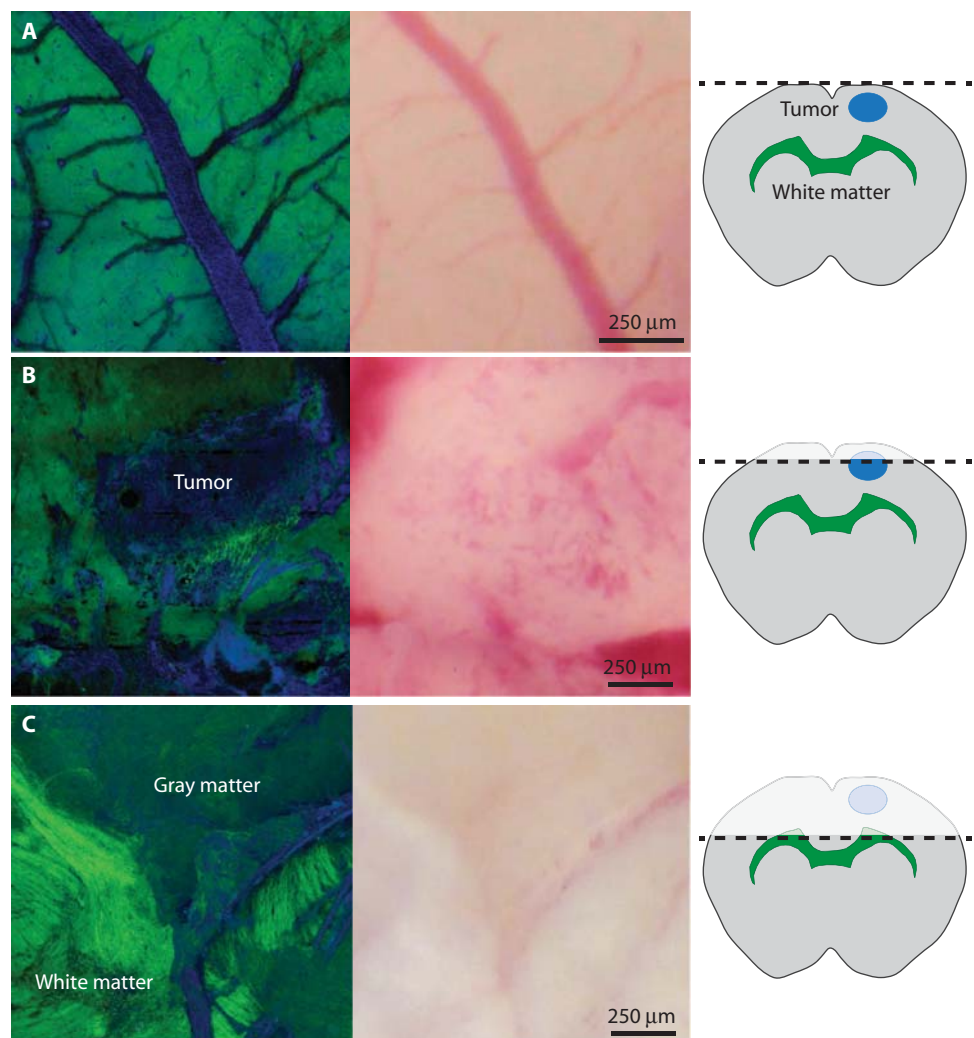


Fig. 6. SRS imaging during simulated tumor resection on mouse brain. *En face*, epi-SRS images were obtained *in vivo* during various stages of a simulated tumor removal. The cartoons on the right show the depth of imaging. (A) In a tumor located beneath the cortical surface, there is no obvious abnormality in SRS (left) or bright-field images (middle) when imaging the cortical surface. (B) After a portion of the cortex has been removed, the tumor is revealed. Blood was present on the dissected surface but did not adversely affect the distinction of tumor-infiltrated regions from non-infiltrated regions. (C) Because dissection was carried deep past the tumor, the normal appearance of white matter and cortex was again visible.

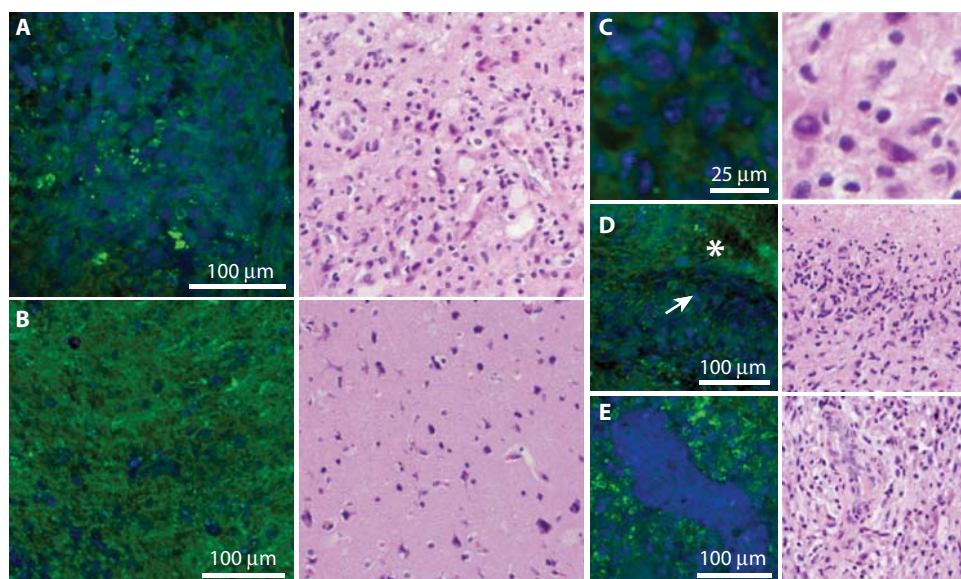


Fig. 7. SRS and H&E microscopy of freshly excised tissue from a human brain tumor. SRS images were obtained from freshly excised human glioblastoma specimen and compared to similar regions in H&E-stained tissue from the same specimen. (A and B) The hypercellularity of viable tumor (A) contrasts with normocellular regions of adjacent brain with minimal tumor infiltration (B). (C to E) Higher-magnification images of the different regions in the specimen demonstrate key diagnostic features of glioblastoma including cellular pleomorphism (C); pseudopalisading necrosis, where densely cellular regions (arrow) border bland, acellular regions of necrosis (asterisk) (D); and microvascular proliferation (E).

SRS offers major advantages over clinically available (and several experimental) dye-based strategies conceived to distinguish normal brain from tumor-infiltrated tissues. Dye-based strategies rely on the extravasation of intravenously administered dyes into a tumor (6, 34). However, the inhomogeneous nature of dye distribution within tumors has been appreciated for decades (22). Moreover, normal nervous tissues and some neoplastic tissues (that is, low-grade glioma) having an intact blood-brain barrier take up little circulating dye and are difficult to image. By probing molecular species that exist in both tumor-infiltrated and non-infiltrated tissues in different concentrations, SRS is not reliant on the delivery of dye for tumor delineation. Consequently, unlike dye-based methods for tumor delineation, SRS microscopy is uniquely well suited for imaging normal, nontumor-infiltrated tissues that should be avoided to minimize surgical morbidity.

Given the fact that glioma cells are known to infiltrate up to 4 cm from the tumor core (35), the goal of glioma surgery is maximal cytoreduction of the mass lesion rather than the removal of all infiltrating tumor cells. However, safely resectable residual tumor is unintentionally left in the operative cavity in the vast majority of glioblastoma surgeries (10). Although the imaging depth of SRS microscopy is limited to 100 μm , it provides a potential means of rapidly defining areas of residual tumor on the surface of a resection cavity during surgeries (Fig. 6). Furthermore, we anticipate that SRS microscopy would be used in an iterative fashion throughout surgery, much in the way intraoperative handheld microscopy is being currently evaluated as a method for evaluating the cellularity of the leading edge of dissection in glioma surgery (36). To evaluate the histoarchitecture of tissues beyond the resection cavity with handheld microscopy, further dissection to expose the tissues of interest is required. We anticipate that the same imaging protocol would be required when handheld SRS microscopy is deployed.

Several engineering challenges, including motion correction and the development of protocols for efficient sampling of a surgical cavity, will be necessary before clinical translation. Current image guidance systems are invaluable for operative planning. However, their navigational accuracy declines as tissues shift during surgery (37). By providing rapid, actionable imaging data from within the operative field, a handheld intraoperative SRS imaging system would enable histology-based image guidance that is immune to navigational errors. Reductions in the average laser pulse power needed to generate SRS images are also possible by optimizing the laser pulse properties, such as pulse duration and repetition rate, improving the likelihood that SRS microscopy will be safe for use in the human brain (fig. S6).

A rigorous evaluation of the performance of SRS microscopy in human brain tumor specimens will be required to accurately judge the feasibility of clinical translation. Nonetheless, here, we provide the first ex vivo human data to demonstrate the feasibility of distinguishing glioblastoma-infiltrated brain from noninfiltrated tissue

(Fig. 7). The ability to extrapolate the performance of SRS microscopy in true surgical conditions based on in vivo imaging in a mouse cranial window model is limited. Among the barriers to intraoperative imaging are the presence of blood within the surgical cavity, the effects of mechanical tissue manipulation by surgical dissection, and motion artifacts. The clinical translation of SRS microscopy will also require the development of a handheld surgical device that can be used to acquire images from within a surgical cavity.

Extent of resection has emerged as one of the most important prognostic factors for many tumors. Yet, the goal of maximizing extent of resection is inconsistently achieved. The studies in mouse models of human GBM presented here suggest that SRS microscopy holds great potential for discriminating tumor tissue from nontumor-infiltrated tissue and may ultimately be used to optimize the surgical treatment of cancer.

MATERIALS AND METHODS

Study design

The central goal of this study was to evaluate the ability of SRS microscopy to image brain tumor infiltration. We began by comparing thin frozen section SRS imaging with standard H&E histopathology in normal mice ($n = 6$) and human glioblastoma xenograft mouse models ($n = 6$). We then quantified the correlation between SRS and H&E tissue imaging through a Web-based survey administered to neuro-pathologists, who were blinded to the tumor infiltration status of the FOVs ($n = 75$) they were grading. Next, we evaluated SRS imaging of fresh tissues in normal mice ($n = 10$) and human glioblastoma mouse models ($n = 6$), first ex vivo, then in vivo. Finally, we used an amendment to the brain tumor bank protocol at the Brigham and

Women's Hospital to procure tissue to evaluate the ability of SRS to image tumor infiltration in human surgical specimens ($n = 1$).

Imaging system

The principles and setup of the SRS microscope have been previously described in detail (13, 28). Briefly, we used a Stokes beam at 1064 nm (picoTRAIN, High Q Laser; 7 ps, 76 MHz) and a tunable pump beam (650 to 1000 nm) from an optical parametric oscillator (Levante Emerald, APE GmbH). The two pulse trains were then spatially and temporally overlapped, aligned into a laser scanning microscope (FV300; Olympus), and focused into the sample. The energy difference between the pump and Stokes photons was tuned to match the energy of a specific molecular vibration to induce an SRS process, resulting in excitation of the ground-state ($v = 0$) molecules to their vibrational excited state ($v = 1$) (Fig. 1A). The intensity loss of the pump beam is the so-called SRL, and the intensity gain of the Stokes beam is the so-called SRG. All SRS images in this work were acquired from SRL, whose spectra have been shown to replicate that of spontaneous Raman scattering (13, 28). To detect the small fraction of SRL signal over the large pump frequency ($\Delta I/I < 10^{-4}$), we modulated the Stokes beam at a high frequency (10 MHz) using an electro-optical modulator, and detected the SRL signal by a homebuilt lock-in amplifier with a time constant of $\sim 1 \mu\text{s}$ (Fig. 1C). We used the fastest imaging speed of the microscope (1 s/frame) for both ex vivo and in vivo experiments.

A specially designed epi-detector was invented by Saar *et al.* (28) to detect the backscattered signal from thick (>1 mm) tissues and live targets. Modifications to this design are described in the Supplementary Methods.

GBM cell line and xenografts

The GBM cell line BT112 was derived from surgical resection material acquired from glioblastoma patients undergoing neurosurgery at the Brigham and Women's Hospital on a protocol approved by their Institutional Review Board (IRB). Briefly, tumor fragments were mechanically dissociated with the MACS Brain Tumor Dissociation Kit (Miltenyi Biotech), and tumorspheres were established according to the manufacturer's protocol. Tumorspheres were propagated in human NeuroCult NS-A Proliferation Media (StemCell Technologies) supplemented with epidermal growth factor, basic fibroblast growth factor (Miltenyi Biotech), and heparin sulfate (StemCell Technologies). BT112 xenografts were generated by injecting 100,000 cells in the right striatum or superficial cortex of severe combined immunodeficient mice (IcrTac:ICR-Prkdcscid; Charles River Labs) and aged under standard conditions.

Fresh mouse tissue preparation

Mice were anesthetized with isoflurane and decapitated. Brains were harvested from freshly sacrificed mice, rinsed with normal saline, and placed in a brain mold. Sections were sliced at 2-mm intervals manually with a razor blade and placed on a microscope slide between two coverslips.

Fresh human brain tumor specimen imaging

Human tissue was procured from a patient undergoing brain tumor resection at the Brigham and Women's Hospital through Partners IRB protocol (#2011P002387). The Partners IRB protocol (#2011 P002387) supports the collection and research utilization of brain tumor tissue collected from all eligible patients at the Brigham and Women's Hospital and Dana-Farber Cancer Institute. The patient ($n = 1$) was informed of the risks of participating in the study during the consent process. A portion of the tissue, in excess of what was needed for histopathologic

diagnosis, was allocated for SRS imaging during surgery. Tissue was then transferred to the imaging laboratory, stored in cold saline, placed on a glass slide, and imaged in transmission mode, as described above.

Statistical analysis

Statistical analysis comparing concordance between H&E and SRS was performed with the κ statistic and its two-sided 95% CI, based on the asymptotic variance of the κ statistic (whose validity is supported by the study's sample size) and the standard normal distribution (38). Analyses were performed with SAS software version 9.2 (SAS Institute Inc.). We assessed the concordance of SRS and H&E microscopy to classify the 75 identical FOVs as being consistent with normal to minimally hypercellular tissue with scattered atypical cells, or infiltrating or dense glioma. The κ statistic is calculated as a measure of agreement between the two methods, with values of <0.40 indicating poor to slight agreement, 0.41 to 0.60 fair to moderate, 0.61 to 0.80 good, and 0.81 to 1.00 very good agreement (39). No multiplicity adjustments were made to the nominal significance level for testing.

SUPPLEMENTARY MATERIALS

www.sciencetranslationalmedicine.org/cgi/content/full/5/201/201ra119/DC1

Methods

- Fig. S1. Raman spectra of brain tissue, lipids, and proteins.
- Fig. S2. Representative infiltrating glioma SRS FOVs correctly classified by neuropathologists.
- Fig. S3. Comparison between transmission and epi-SRS images.
- Fig. S4. Comparison of SRS images in fresh and frozen tissues.
- Fig. S5. SRS images of various mouse models of human brain tumors.
- Fig. S6. Power scaling of SRS microscopy.
- Fig. S7. Additional in vivo SRS images of GBM xenografts.
- Fig. S8. Coronal H&E staining after in vivo imaging.
- Table S1. Compiled contingency table summarizing survey results.
- Movie S1. Three-dimensional depth profile of brain tumor margin.

REFERENCES AND NOTES

1. W. E. Dandy, Removal of right cerebral hemisphere for certain tumors with hemiplegia: Preliminary report. *JAMA* **90**, 823–825 (1928).
2. J. M. Nazzaro, E. A. Neuwelt, The role of surgery in the management of supratentorial intermediate and high-grade astrocytomas in adults. *J. Neurosurg.* **73**, 331–344 (1990).
3. M. E. Sughrae, A. J. Kane, G. Shangari, M. J. Rutkowski, M. W. McDermott, M. S. Berger, A. T. Parsa, The relevance of Simpson grade I and II resection in modern neurosurgical treatment of World Health Organization grade I meningiomas. *J. Neurosurg.* **113**, 1029–1035 (2010).
4. S. N. Kalkanis, D. Kondziolka, L. E. Gaspar, S. H. Burri, A. L. Asher, C. S. Cobbs, M. Ammirati, P. D. Robinson, D. W. Andrews, J. S. Loeffler, M. McDermott, M. P. Mehta, T. Mikkelsen, J. J. Olson, N. A. Paleologos, R. A. Patchell, T. C. Ryken, M. E. Linskey, The role of surgical resection in the management of newly diagnosed brain metastases: A systematic review and evidence-based clinical practice guideline. *J. Neurooncol.* **96**, 33–43 (2010).
5. M. Lacroix, D. Abi-Said, D. R. Fourney, Z. L. Gokaslan, W. Shi, F. DeMonte, F. F. Lang, I. E. McCutcheon, S. J. Hassenbusch, E. Holland, K. Hess, C. Michael, D. Miller, R. Sawaya, A multivariate analysis of 416 patients with glioblastoma multiforme: Prognosis, extent of resection, and survival. *J. Neurosurg.* **95**, 190–198 (2001).
6. N. Sanai, M. Y. Polley, M. W. McDermott, A. T. Parsa, M. S. Berger, An extent of resection threshold for newly diagnosed glioblastomas. *J. Neurosurg.* **115**, 3–8 (2011).
7. J. S. Smith, E. F. Chang, K. R. Lamborn, S. M. Chang, M. D. Prados, S. Cha, T. Tihan, S. Vandenberg, M. W. McDermott, M. S. Berger, Role of extent of resection in the long-term outcome of low-grade hemispheric gliomas. *J. Clin. Oncol.* **26**, 1338–1345 (2008).
8. W. Stummer, U. Pichlmeier, T. Meinel, O. D. Wiestler, F. Zanella, H. J. Reulen: ALA-Glioma Study Group, Fluorescence-guided surgery with 5-aminolevulinic acid for resection of malignant glioma: A randomised controlled multicentre phase III trial. *Lancet Oncol.* **7**, 392–401 (2006).
9. F. K. Albert, M. Forsting, K. Sartor, H. P. Adams, S. Kunze, Early postoperative magnetic resonance imaging after resection of malignant glioma: Objective evaluation of residual tumor and its influence on regrowth and prognosis. *Neurosurgery* **34**, 45–60; discussion 60–61 (1994).
10. D. Orringer, D. Lau, S. Khatri, G. J. Zamora-Berridi, K. Zhang, C. Wu, N. Chaudhary, O. Sagher, Extent of resection in patients with glioblastoma: Limiting factors, perception of resectability, and effect on survival. *J. Neurosurg.* **117**, 851–859 (2012).

11. A. Zumbusch, G. R. Holtom, X. S. Xie, Three-dimensional vibrational imaging by coherent anti-Stokes Raman scattering. *Phys. Rev. Lett.* **82**, 4142–4145 (1999).
12. C. L. Evans, X. S. Xie, Coherent anti-stokes Raman scattering microscopy: Chemical imaging for biology and medicine. *Annu. Rev. Anal. Chem.* **1**, 883–909 (2008).
13. C. W. Freudiger, W. Min, B. G. Saar, S. Lu, G. R. Holtom, C. He, J. C. Tsai, J. X. Kang, X. S. Xie, Label-free biomedical imaging with high sensitivity by stimulated Raman scattering microscopy. *Science* **322**, 1857–1861 (2008).
14. P. Nandakumar, A. Kovalev, A. Volkmer, Vibrational imaging based on stimulated Raman scattering microscopy. *New J. Phys.* **11**, 033026 (2009).
15. Y. Ozeki, F. Dake, S. Kajiyama, K. Fukui, K. Itoh, Analysis and experimental assessment of the sensitivity of stimulated Raman scattering microscopy. *Opt. Express* **17**, 3651–3658 (2009).
16. E. Ploetz, S. Laimgruber, S. Berner, W. Zinth, P. Gilch, Femtosecond stimulated Raman microscopy. *Appl. Phys. B* **87**, 389–393 (2007).
17. D. Fu, F. K. Lu, X. Zhang, C. Freudiger, D. R. Pernik, G. Holtom, X. S. Xie, Quantitative chemical imaging with multiplex stimulated Raman scattering microscopy. *J. Am. Chem. Soc.* **134**, 3623–3626 (2012).
18. Y. Fu, T. B. Huff, H. W. Wang, H. Wang, J. X. Cheng, Ex vivo and in vivo imaging of myelin fibers in mouse brain by coherent anti-Stokes Raman scattering microscopy. *Opt. Express* **16**, 19396–19409 (2008).
19. Y. Yang, F. Li, L. Gao, Z. Wang, M. Thrall, S. Shen, K. Wong, S. T. C. Wong, Differential diagnosis of breast cancer using quantitative, label-free and molecular vibrational imaging. *Biomed. Opt. Express* **2**, 2160–2174 (2011).
20. C. W. Freudiger, R. Pfannl, D. A. Orringer, B. G. Saar, M. B. Ji, Q. Zeng, L. Ottoboni, Y. Wei, C. Waeber, J. R. Sims, P. L. De Jager, O. Sagher, M. A. Philbert, X. Y. Xu, S. Kesari, X. S. Xie, G. S. Young, Multicolored stain-free histopathology with coherent Raman imaging. *Lab. Invest.* **92**, 1492–1502 (2012).
21. X. Zhang, M. B. J. Roelfaers, S. Basu, J. R. Daniele, D. Fu, C. W. Freudiger, G. R. Holtom, X. S. Xie, Label-free live-cell imaging of nucleic acids using stimulated Raman scattering microscopy. *Chemphyschem* **13**, 1054–1059 (2012).
22. G. E. Moore, Fluorescein as an agent in the differentiation of normal and malignant tissues. *Science* **106**, 130–131 (1947).
23. D. A. Dombeck, K. A. Kasischke, H. D. Vishwasrao, M. Ingelsson, B. T. Hyman, W. W. Webb, Uniform polarity microtubule assemblies imaged in native brain tissue by second-harmonic generation microscopy. *Proc. Natl. Acad. Sci. U.S.A.* **100**, 7081–7086 (2003).
24. S. Witte, A. Negrean, J. C. Lodder, C. P. J. de Kock, G. Testa Silva, H. D. Mansvelder, M. Louise Groot, Label-free live brain imaging and targeted patching with third-harmonic generation microscopy. *Proc. Natl. Acad. Sci. U.S.A.* **108**, 5970–5975 (2011).
25. C. L. Evans, X. Xu, S. Kesari, X. S. Xie, S. T. C. Wong, G. S. Young, Chemically-selective imaging of brain structures with CARS microscopy. *Opt. Express* **15**, 12076–12087 (2007).
26. C. Pohling, T. Backup, A. Pagenstecher, M. Motzkus, Chemoselective imaging of mouse brain tissue via multiplex CARS microscopy. *Biomed. Opt. Express* **2**, 2110–2116 (2011).
27. C. L. Evans, E. O. Potma, M. Puoris'haag, D. Côté, C. P. Lin, X. S. Xie, Chemical imaging of tissue in vivo with video-rate coherent anti-Stokes Raman scattering microscopy. *Proc. Natl. Acad. Sci. U.S.A.* **102**, 16807–16812 (2005).
28. B. G. Saar, C. W. Freudiger, J. Reichman, C. M. Stanley, G. R. Holtom, X. S. Xie, Video-rate molecular imaging in vivo with stimulated Raman scattering. *Science* **330**, 1368–1370 (2010).
29. N. G. Horton, K. Wang, D. Kobat, C. G. Clark, F. W. Wise, C. B. Schaffer, C. Xu, In vivo three-photon microscopy of subcortical structures within an intact mouse brain. *Nat. Photonics* **7**, 205–209 (2013).
30. D. N. Louis, H. Ohgaki, O. D. Wiestler, W. K. Cavenee, *WHO Classification of Tumours of the Central Nervous System* (IARC, Lyon, 2007).
31. J. Cohen, A coefficient of agreement for nominal scales. *Educ. Psychol. Meas.* **20**, 37–46 (1960).
32. S. Mehta, E. Huillard, S. Kesari, C. L. Maire, D. Golebiowski, E. P. Harrington, J. A. Alberta, M. F. Kane, M. Theisen, K. L. Ligon, D. H. Rowitch, C. D. Stiles, The central nervous system-restricted transcription factor Olig2 opposes p53 responses to genotoxic damage in neural progenitors and malignant glioma. *Cancer Cell* **19**, 359–371 (2011).
33. C. Nimsy, O. Ganslandt, M. Buchfelder, R. Fahlbusch, Glioma surgery evaluated by intraoperative low-field magnetic resonance imaging. *Acta Neurochir. Suppl.* **85**, 55–63 (2003).
34. M. F. Kircher, A. de la Zerda, J. V. Jokerst, C. L. Zavaleta, P. J. Kempen, E. Mittra, K. Pitter, R. Huang, C. Campos, F. Habte, R. Sinclair, C. W. Brennan, I. K. Mellingshoff, E. C. Holland, S. S. Gambhir, A brain tumor molecular imaging strategy using a new triple-modality MRI-photoacoustic-Raman nanoparticle. *Nat. Med.* **18**, 829–834 (2012).
35. D. L. Silbergeld, M. R. Chicoine, Isolation and characterization of human malignant glioma cells from histologically normal brain. *J. Neurosurg.* **86**, 525–531 (1997).
36. N. Sanai, J. Eschbacher, G. Hattendorf, S. W. Coons, M. C. Preul, K. A. Smith, P. Nakaji, R. F. Spetzler, Intraoperative confocal microscopy for brain tumors: A feasibility analysis in humans. *Neurosurgery* **68**, 282–290 (2011).
37. A. Nabavi, P. M. Black, D. T. Gering, C. F. Westin, V. Mehta, R. S. Pergolizzi Jr., M. Ferrar, S. K. Warfield, N. Hata, R. B. Schwartz, W. M. Wells III, R. Kikinis, F. A. Jolesz, Serial intraoperative magnetic resonance imaging of brain shift. *Neurosurgery* **48**, 787–797; discussion 797–798 (2001).
38. J. L. Fleiss, J. Cohen, B. S. Everitt, Large sample standard errors of kappa and weighted kappa. *Psychol. Bull.* **72**, 323–327 (1969).
39. J. R. Landis, G. G. Koch, The measurement of observer agreement for categorical data. *Biometrics* **33**, 159–174 (1977).

Acknowledgments: We thank B. Saar for technical support, I. Terumasa for help with data analysis, G. Barkhoudarian and D. Tavaniepour for their assistance with image grading, H. Wagner for her expertise in editing the manuscript, and S. Riddle for his illustrations. **Funding:** This work was supported by the NIH Director's Transformative Research Award Program T-R01 (1R01EB010244-01 to X.S.X.) and NIH grants R25CA089017 (to D.A.O.) and P01CA095616 (K.L.L.). **Author contributions:** X.S.X., C.W.F., M.J., and D.A.O. conceived the project; X.S.X., C.W.F., M.J., D.A.O., A.J.G., N.Y.R.A., G.S.Y., and O.S. contributed to experimental design; M.J. and D.A.O. performed the experiments; S.R., M.H., and K.L.L. created tumor models; S.R., S.S., K.L.L., and S.C.-P. performed image classification and interpretation; I.N. created the Web-based survey; X.L. sectioned and stained tissue sections; M.J., D.A.O., D.L., and C.S. performed the statistical analysis of the data; D.A.O., M.J., C.W.F., and X.S.X. wrote the manuscript. **Competing interests:** The authors declare that they have no competing interests. **Data and materials availability:** A Uniform Biological Materials Transfer Agreement, executed on 20 October 2011 between Dana-Farber Cancer Institute and Harvard University, was put in place to govern the transfer of human GBM xenograft-bearing mice to Harvard for SRS imaging. A Partners IRB protocol (#2011P002387) was approved for human brain tumor specimen imaging at Harvard University. To obtain these samples, contact X.S.X.

Submitted 19 February 2013
 Accepted 7 August 2013
 Published 4 September 2013
 10.1126/scitranslmed.3005954

Citation: M. Ji, D. A. Orringer, C. W. Freudiger, S. Ramkissoon, X. Liu, D. Lau, A. J. Golby, I. Norton, M. Hayashi, N. Y. R. Agar, G. S. Young, C. Spino, S. Santagata, S. Camelo-Piragua, K. L. Ligon, O. Sagher, X. S. Xie, Rapid, label-free detection of brain tumors with stimulated Raman scattering microscopy. *Sci. Transl. Med.* **5**, 201ra119 (2013).